SCIENCE CHINA Materials ARTICLES

mater.scichina.com link.springer.com

Published online 4 January 2021 | https://doi.org/10.1007/s40843-020-1538-6
Sci China Mater 2021, 64(6): 1495–1506

Photodirected 2D-to-3D morphing structures of shape memory polycaprolactone/$W_{18}O_{49}$ nanowires composite film

Guangming Tian[1], Guangming Zhu[1*], Shuogui Xu[2], Ming Li[3] and Renjie Tian[1]

ABSTRACT **Shape memory materials possess programmable complex and large deformations towards external stimuli, which are particularly essential for their potential applications. For the transformation of planar two-dimensional (2D) structures into complex 3D structures, the design of asymmetric or bilayer thin sheets is usually required. In this paper, we propose a facile strategy to achieve these complex 3D structures that can be transformed to various pre-determined shapes sequentially by laser-triggered site-specific deformations. The response of shape memory polycaprolactone (PCL) to laser is realized by physically doping $W_{18}O_{49}$ nanowires into the cross-linked PCL diacrylate matrix. When irradiated by 98 mW cm^{-2} laser, the pre-stretched PCL/$W_{18}O_{49}$ film shows an out-of-plane bending deformation due to the temperature gradient and single-domain orientation on the thickness between the upper layer and lower layer. The bending rates and amplitudes of the film can be tailored by adjusting the parameters of irradiation time, the film thickness as well as the pre-stretch strain. Remarkably, the pre-stretched film can automatically bend in more intricate complex deformations by integration with kirigami cuts in planar. Finally, we demonstrate that by activating the dynamic transesterification reaction within the same film, it can also achieve the 2D-to-3D transformations. With these decent features, this kind of novel PCL//$W_{18}O_{49}$ film shows great potential in the field of biomedical devices or soft robotics.**

Keywords: Shape memory materials, laser-triggered, temperature gradient, bending deformation, dynamic transesterification reaction

INTRODUCTION

Shape memory materials (SMPs) are considered as a sort of intelligent materials which could memorize the deformed shape and then recover to the original shape upon external stimuli, such as heat [1], light [2], and electricity [3]. Nowadays, SMPs have been applied in many fields ranging from soft actuators [4], biomedical engineering [5], aerospace [6] to flexible electronic devices [7]. Of all SMPs, polycaprolactone (PCL) has gained ever-increasing interest over the past decade [8–10]. For the semi-crystalline PCL, the switching temperature is generally defined by its melting temperature [11], which in most cases can be extensively tailored from the perspective of molecular architecture [12–14]. In view of its distinctive merits, PCL has been given particular focus on various fields [15–17].

However, many practical applications require PCL with complex shapes and large deformations. Currently, the origami and kirigami have emerged as a new technique to create complex configuration from two-dimensional (2D) sheets by accurately folding predefined creases or cutting, and the past decade has witnessed surging studies on applying origami and kirigami concept to the complex shape morphing of PCL [18–20]. Besides that, the design of bilayer thin sheets is also a promising strategy to endow materials with 3D complex transformations [21–23]. The drawback of this method is that the layered structures cannot be fabricated using traditional ways, and a strong enough adhesive force between the layers must be guaranteed to prevent abscission during deformation. On the other aspect, surface pattern is a good way to guide the materials to undergo shape transformation into a pre-

[1] Department of Applied Chemistry, School of Science, Northwestern Polytechnical University, Xi'an 710072, China
[2] Emergency Medicine Department & Trauma Emergency Center, Changhai Hospital, Second Military Medical University, Shanghai 200433, China
[3] Department of Applied Physics, School of Science, Northwestern Polytechnical University, Xi'an 710072, China
* Corresponding author (email: gmzhu@nwpu.edu.cn)

programmed structure [24–28]. Besides that, new surging thermadapt SMPs can also transform a 2D film into geometrically complex shape by combining solid state plasticity and elasticity [29,30]. This method is favorable and pioneering but cannot be remotely realized. Under such circumstance, light is the most attractive choice since it can be halted and resumed at any time [31]. The light-responsive shape memory effect can be achieved by incorporating the light absorbers into the cross-linked networks. Many additives such as carbon-based materials [32–34], dye [35], plasmonic materials [36,37] and WO_{3-x} nanocrystals [38] have already been proved as excellent photothermal agents.

In this study, we conduct a comprehensive study on the feasibility of using laser for the PCL 2D-to-3D transformation. To achieve it, we resort to thiol-ene reaction for synthesizing PCL cross-linked network; the incorporation of $W_{18}O_{49}$ nanowires into cross-linked network endows the composite films with light responsiveness. Specifically, we pre-stretch the PCL/$W_{18}O_{49}$ composite film to a certain length above its melting temperature and then freeze the internal stress. When a certain area of the composite film is subjected to laser irradiation, the incorporated $W_{18}O_{49}$ nanowires absorb the light and enable rapid temperature increase over the melting temperature of PCL and trigger the upper layer contraction. On the other hand, the lower layer of the composite film is still in its glass state, thus actuating the pre-stretched PCL/$W_{18}O_{49}$ composite film with bending deformation (Scheme 1b). Further, we systematically investigate the effects of laser intensity, film thickness and irradiation time on the bending angles of pre-stretched composite films. Based on the results of bending amplitudes and the integrated kirigami technique, various complicated yet predictable 3D configurations are obtained. Finally, we demonstrate that the 2D-to-3D transformation can also be achieved by activating the dynamic covalent bond within the same polymer network. This photo-actuated PCL/$W_{18}O_{49}$ composite film has many advantages compared with the reported materials, such as remote triggering, 2D-to-3D transformations rather than 3D-to-2D transformations, and large shape morphing structures.

EXPERIMENTAL SECTION

Materials

PCL diol with a number-average molecular weight (M_n) of 4000 was purchased from Shenzhen Esun Industrial Co.Ltd, China. Acryloyl chloride, triethylamine (TEA), pentaerythritol tetrakis (3-mercaptopropionate), and all other organic reagents were supplied by Macklin. Tungsten chloride particles (WCl_6) were purchased from Aladdin Reagent. Oligo poly(ethylene glycol) (PEG, M_n = 400, PEG-400) was supplied by Macklin. Unless otherwise stated, all the reagents were used without further purification.

Synthesis of PEGylated $W_{18}O_{49}$ nanowires

The PEGylated $W_{18}O_{49}$ nanowires were synthesized according to the previous reported literature [39]. Typically, WCl_6 (0.2 g) was firstly dissolved in a mixture of 50 mL of PEG 400 and ethanol with a volume ratio of 7:3. Then the mixed solution was treated under ultrasonication and a transparent yellow solution was obtained. The resultant yellow solution was then transferred to a poly(tetrafluoroethylene) (Teflon)-lined stainless steel autoclave, sealed, and treated at 180°C for 24 h. The resulting blue precipitate was then subjected to centrifugation and washed with ethanol thrice to fully remove the surface PEG. Finally, the precipitate (PEGylated $W_{18}O_{49}$ nanowires) was dried in vacuum at 50°C for 24 h.

Synthesis of PCL diacrylate (PCLDA)

The PCLDA was synthesized according to our previous reported literature [40]. PCLDA was obtained by end-functionalization of PCL diol with acryloyl chloride. Typically, a mass of 20 g PCL 4000 diol was first dissolved in 60 mL tetrahydrofuran (THF) under ultrasonic vibration until a transparent solution formed, and then 2.4 mL TEA and 1.8 mL acryloyl chloride were added dropwise. The mixture was then magnetically stirred for another 24 h at room temperature, the byproduct was removed by filtration and the polymer was precipitated in excess hexane. The final product was obtained by vacuum drying at 40°C for 24 h prior to use.

Synthesis of the films with and without $W_{18}O_{49}$ nanowires

The PCL cross-linked network was synthesized by thiol-ene click chemistry. Typically, the as-synthesized PCLDA matrix (0.5 g) containing different amounts of $W_{18}O_{49}$ nanowires (χ wt% with respect to PCLDA) was mixed in THF and constantly stirred for 45 min, and then the tetrathiol cross-linker, photoinitiator (2 wt% 2,2-dimethoxy-2-phenylacetophenone (DMPA) relative to PCLDA) was added to the mixed PCLDA/$W_{18}O_{49}$ solution and stirred for another 30 min until getting homogeneous. The mixture was subsequently injected into a glass mold separated by a specific thickness and then irradiated under 365-nm UV light. The obtained samples were then vacuum-dried overnight. The sample without

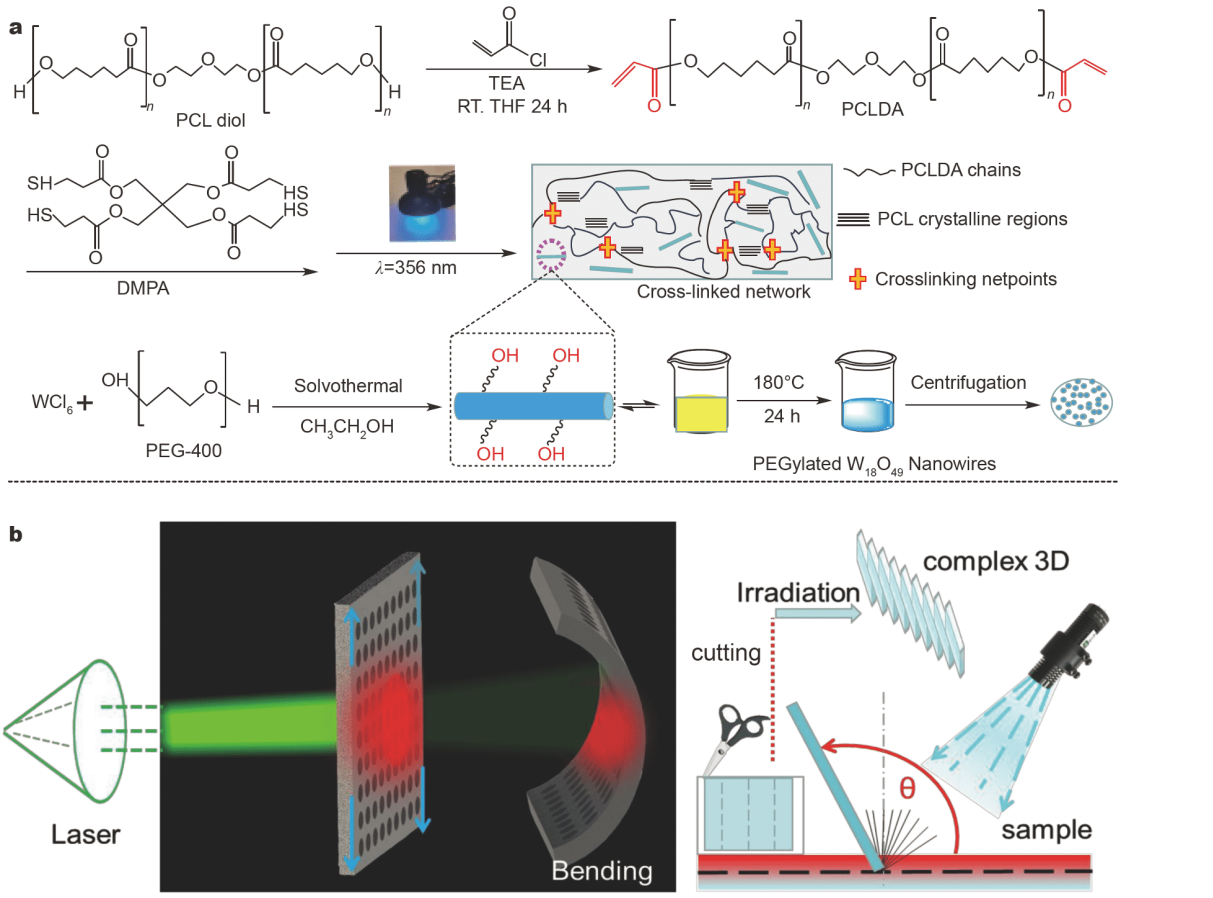

Scheme 1 Schematic illustration of the fabrication route for PCL/$W_{18}O_{49}$ composite films (a) and the corresponding representation of bending deformation behaviors as well as complex 3D structures (b).

$W_{18}O_{49}$ nanowires was described as pure cPCL. The composite films containing χ wt% $W_{18}O_{49}$ nanowires were marked as PCL-$W_{18}O_{49}$-χ for simplicity.

Characterizations

Fourier transform infrared spectroscopy (FT-IR) (DSOR 27, Bruck, Germany) was employed to capture the surface chemical groups. The crystallization temperature (T_c) and melting temperature (T_m) as well as the crystallinity of the composite film were measured by differential scanning calorimeter (DSC). The sample with a mass ranging from 5 to 8 mg encapsulated into a sealed pan was first heated from 10 to 100°C at a rate of 10°C min^{-1} under a nitrogen atmosphere and held at 100°C for 3 min to eliminate the prior thermal history, and then the samples were cooled down to 10°C at a rate of 10°C min^{-1} to record the crystallization behavior and reheated to 100°C again to record the melting behavior. The crystallinity of each sample was calculated using the following Equation (1),

$$X_C(\%) = (\Delta H_m/\Delta H_m^0) \times 100\%, \quad (1)$$

where ΔH_m^0 is the theoretical enthalpy (136.5 J g^{-1}) for fusion of 100% crystalline PCL. Enthalpy change (ΔH_m) of PCL was determined from the endothermic peak.

Transmission electron microscopy (TEM) images were recorded using FEI Talos-F200X instrument. Simply, a drop of the sample dispersed in ethanol was dropcast on a copper grid and dried in the open atmosphere to observe the morphology of $W_{18}O_{49}$ nanowires. Shape memory cycles were tested using a Netzsch DMA 242E. The sample was first loaded at room temperature, heated to 70°C, and then the sample was elongated to a certain extension (ε_m) under a proper loading. The sample was cooled to 0°C before releasing the loaded force, upon which the sample strain was ε_{dload}. Then, the force was removed and the fixed strain of the sample was ε_d. Finally, the sample was reheated to 70°C, upon which the sample got recovered and the strain decreased to ε_{rec}. The shape memory fixity ratio (R_f) and shape recovery ratio (R_r)

were calculated by the following Equations (2) and (3):

$$R_f = \varepsilon_d/\varepsilon_{dload} \times 100\%, \quad (2)$$

$$R_r = (\varepsilon_d - \varepsilon_{rec})/\varepsilon_d \times 100\%. \quad (3)$$

Besides the stretching mode, a bending–recovery test was also performed to characterize the shape memory properties. First, a sample was bent into a U-shape at 60°C with an initial angle of θ_0 and the temporary shape was obtained by cooling the sample to room temperature under an external load. After the external load was removed, the temporarily fixed angle was recorded as θ_1. Then the deformed sample was reheated to 60°C or irradiated by laser to recover the shape and the final angle was recorded as θ_2. The whole recovery process was recorded using a semicircle meter. The R_f and R_r were calculated according to the following Equations (4) and (5).

$$R_r = (\theta_0 - \theta_2)/\theta_0 \times 100\%, \quad (4)$$

$$R_f = \theta_1/\theta_0 \times 100\%. \quad (5)$$

A 532 nm laser (Oxlasers) with different intensity was used to irradiate the site-specific composite film, and a photo-radiometer (OPHIR NOVA II) was employed for testing the laser intensity. The increasing temperature of composite films caused by laser irradiation was traced by thermal infrared camera (Fluke Ti200). Light-induced bending deformation was recorded by using a digital camera in iPhone 6.

RESULTS AND DISCUSSION

Structural characterization of the as-synthesized $W_{18}O_{49}$ nanowires

$W_{18}O_{49}$ nanowires were prepared by hydrothermal reaction. When ethanol was only used as the solvent, the length of $W_{18}O_{49}$ nanowires reaches several micrometers as shown in Fig. 1a, b and Fig. S1. Fig. 1c and Fig. S2 show the elemental mapping of $W_{18}O_{49}$ nanowires. Three elements, W, O, and Cl, coexist and are evenly distributed, and the existence of Cl might be due to the unsound crystal that has not fully grown. The as-obtained $W_{18}O_{49}$ nanowires are too long for biological application and its photothermal conversion would be influenced to a large extent [37]. When the PEG-400 and ethanol are mixed together with a volume ratio of 7:3 to prepare $W_{18}O_{49}$

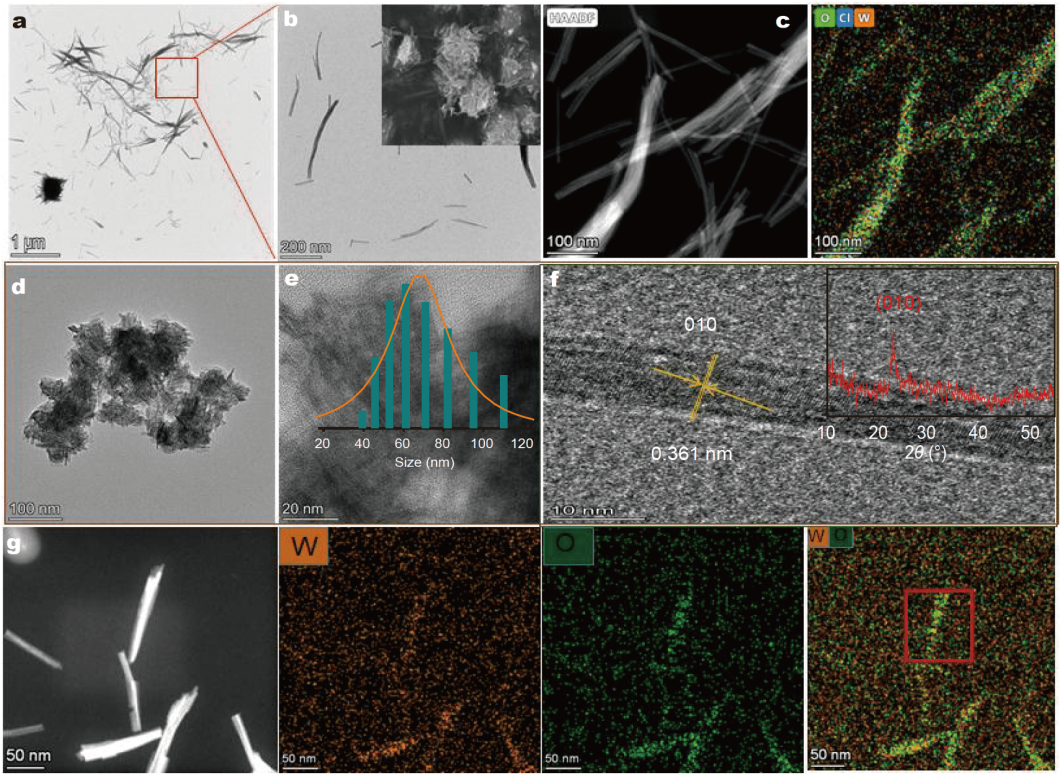

Figure 1 Structural characterization of the as-synthesized $W_{18}O_{49}$ nanowires and PEGylated $W_{18}O_{49}$ nanowires. (a, b) TEM images of $W_{18}O_{49}$ nanowires. (c) Element mapping. (d, e) PEGylated $W_{18}O_{49}$ nanowires; inset shows the size distribution. (f) HRTEM image; inset shows the XRD spectrum. (g) Element mapping of PEGylated $W_{18}O_{49}$ nanowires.

nanowires, the length of nanowires sharply shortens to about 70 nm (Fig. 1d, e), which is favorable for photothermal conversion and their biocompatibility properties. In the inset of Fig. 1e, the size distribution of PEGylated $W_{18}O_{49}$ nanowires is mainly in the range of 50–90 nm, which is in line with the data obtained from TEM image of Fig. 1d. High-resolution TEM (HRTEM) image of a single nanowire is shown in Fig. 1f and the distance between the adjacent lattice fringes is 0.361 nm, in good agreement with the lattice fringes of the (010) plane of $W_{18}O_{49}$ crystals, indicating that the PEGylated $W_{18}O_{49}$ nanowire grows along the 010 direction [39]. The growing direction is in line with the crystal plane of (010) at 2θ = 23.12° obtained from the XRD pattern (Fig. 1f inset). Fig. 1g shows the elemental mapping of PEGylated $W_{18}O_{49}$ nanowires, where W (yellow) and O (green) coexist with even distribution. Besides, the FTIR in Fig. 2a confirms the presence of PEG ligands on the surface of PEGylated $W_{18}O_{49}$ nanowires. The characteristic band at about 3450 cm^{-1} is attributed to the stretching vibration of –OH group in PEG-400 or absorbed water [41]; at the same time, the new transmission bands at 2852 cm^{-1} and 2922 cm^{-1} are respectively ascribed to the stretching vibrations of methylene ($-CH_2$) units in PEG-400 chain, and the band at about 1097 cm^{-1} is corresponding to C–O–C stretching vibration coordinated to metal cations, which shifts about 9 cm^{-1} to lower wavenumber compared with the IR spectrum of pure PEG-400 (1116 cm^{-1}), further proving the formation of the chemical bonds between inorganic $W_{18}O_{49}$ nanowires and PEG-400. Consequently, it can be concluded that there exist PEG-ligands on the surface of $W_{18}O_{49}$ nanowires, suggesting the successful preparation of PEGylated $W_{18}O_{49}$ nanowires.

Characterization of PCLDA/$W_{18}O_{49}$ nanowires composite film

As shown in Scheme 1a, PCLDA matrix, blue PEGylated $W_{18}O_{49}$ nanowire precipitate and tetrathiol cross-linker could be photopolymerized upon 365 nm UV irradiation. For the characterization of PCL diol and PCLDA, we used the FTIR and ^1H NMR to illustrate the modification of the active double bond. Compared with the spectrum of PCL diol in Fig. 2a, the new absorption bands at 813 and 1635 cm^{-1} in the spectrum of PCLDA are assigned to the C=C bond, suggesting that the carbon-carbon double bond is successfully grafted onto the end of PCL chains [42]. Meanwhile, the characteristic hydroxyl peak in PCL diol at 3540 cm^{-1} is totally consumed during the formation of PCLDA, further demonstrating the reaction of hydroxyl in PCL diol with acryloyl chloride. The FTIR spectrum of PCL/$W_{18}O_{49}$ composite film shows that the C=C stretching peak at 1634 cm^{-1} almost disappeared after photopolymerization, indiating that the PCLDA underwent a high degree of cross-linking reaction. Also, after introducing PEGylated $W_{18}O_{49}$ nanowires into PCLDA matrix, the C=O stretch peak shifts slightly to lower wavenumber. ^1H NMR (Fig. S3) in the range of 5.8–6.5 ppm also confirms the existence of C=C bond, which is consistent with the previous report [43]. Here, the acrylation in the PCL diol affects the crystallinity and the ultimate performance of the materials [44]. After PCLDA was successfully photo-crosslinked, we used the gel fraction of samples to reflect the degree of acrylation (Table S1). If the two ends of PCL diol are not linked by C=C bond, the gel fraction test will dissolve this part of molecules. The test shows that the values of all samples were nearly more than 80%, indicating the formation of sufficient cross-linked netpoints in composite films. This

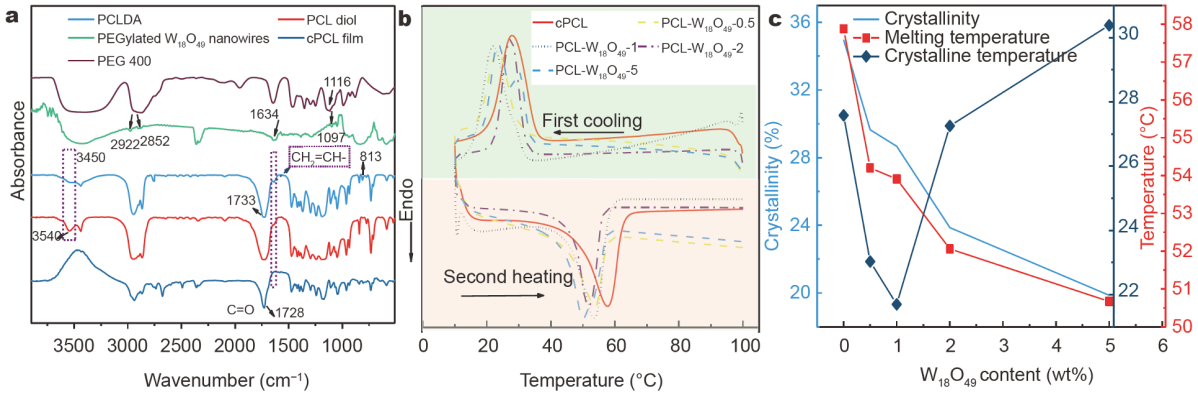

Figure 2 Characterization of the composite films. (a) FTIR image of PEG 400, PEGylated $W_{18}O_{49}$ nanowires, PCL diol, PCLDA and PCL/$W_{18}O_{49}$ composite film. (b) DSC image of pure cPCL and its corresponding composite films. (c) The melting temperature, crystalline temperature, crystallinity for PCL/$W_{18}O_{49}$ nanowires composite film with various PEGylated $W_{18}O_{49}$ nanowires loading contents.

result evidences that the reaction of PCLDA with tetrathiols proceeds to a high conversion.

The melting temperature (T_m) and crystallization temperature (T_c) of the composite film were characterized by DSC. For semi-crystalline shape memory PCL, T_m is generally considered as T_{trans} to trigger the shape change. T_m and T_c (Fig. 2c) were both calculated from the peak top of the DSC curves in Fig. 2b. The results show that increasing the content of PEGylated $W_{18}O_{49}$ nanowires could lower the T_m of composite films. Meanwhile, T_c decreases to 21.7°C, and then increases with the increment of PEGylated $W_{18}O_{49}$ nanowires to 5% due to the confined crystallization and heterogeneous nucleation. When the content of nanowires increases from 0.5% to 5%, the $W_{18}O_{49}$ nanowires might exert a physical restriction on the chains' mobility, which leads to the reduction of T_c. On the other hand, as the content of PEGylated $W_{18}O_{49}$ nanowires continues to increase, they may act as an efficient nucleating agent to accelerate the crystallization, which results in an increasing tendency of T_c [45]. Besides, the crystallinity (X_c) increases from 33.97% to 38.86%, indicating the good compatibility of PEGylated $W_{18}O_{49}$ nanowires with cPCLDA.

Photothermal behaviors of the PCLDA/$W_{18}O_{49}$ nanowires composite films

For the photothermal behavior of the composite films, we first characterized the optical property of the $W_{18}O_{49}$ nanowires using UV-vis-NIR spectroscopy. As the surface of the PEGylated $W_{18}O_{49}$ nanowires has been modified by many PEG-400 ligands, PEGylated $W_{18}O_{49}$ nanowires are hydrophilic and could be soluble in water with stability. Fig. 3a and inset show that the aqueous solution of nanowires displays a blue color and has a strong absorption in the UV and NIR region with the spectrum similar to the previous reported $W_{18}O_{49}$ nanowires [38]. The strong photoabsorption of PEGylated $W_{18}O_{49}$ nanowires enables us to investigate the photothermal effect in the composite film. As seen in Fig. 3b inset, the cross-linked films present deep blue color as the content of nanowires increase. And the SEM images (Fig. S4) show homogeneous dispersion of nanowires in the PCLDA matrix. Then we studied the effect of the content of $W_{18}O_{49}$ nanowires and laser intensity on the temperature of the film surface. As shown in Fig. 3b, the pure cPCL basically has no response to laser at all, the composite film with a low content of 0.5% $W_{18}O_{49}$ nanowires shows a high photoabsorption, and when the content of nanowires increases from 0.5% to 2%, the corresponding surface temperature increases from 54.3 to 69.5°C. However, the surface temperature is almost independent of the nanowire concentration with further adding of 5% nanowires, because too many nanowires gathering on the surface of the film could absorb a lot of heat, but at the same time, dissipate a large amount of heat, leading to the photothermal balance, and thus the $W_{18}O_{49}$ nanowire content has a slight effect on the surface temperature of the composite film. Fig. 3c shows that higher laser intensity could lead to a faster temperature rise. At the same time, we note that the localized temperature of the films can be raised to above 60°C upon laser irradiation, which reaches the melting temperature of PCL and therefore can trigger the shape recovery and deformation of the films.

Shape memory properties and photodirected programmable deformations of the films

To characterize the heat-induced shape memory behaviors of the films, the PCL-$W_{18}O_{49}$-2 was performed with

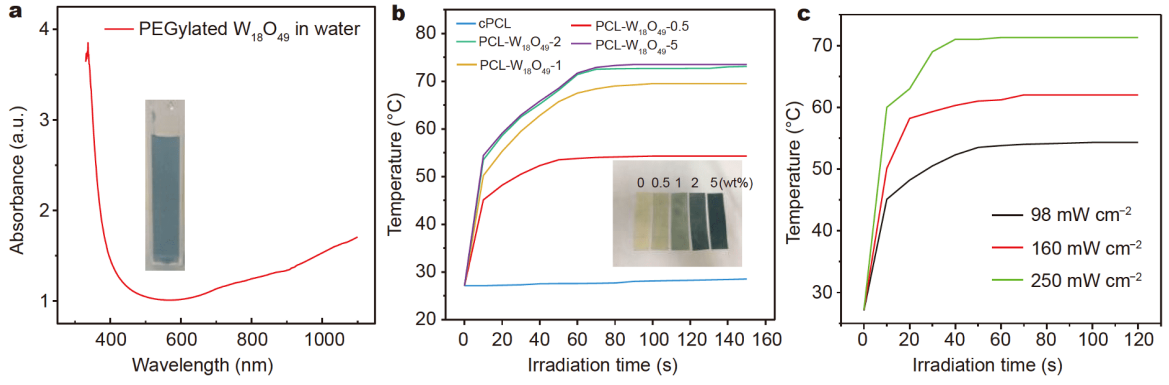

Figure 3 (a) UV-vis-NIR spectra of PEGylated $W_{18}O_{49}$ nanowires aqueous solution at a concentration of 1mg mL^{-1}. (b) Temperature-time curves of films with different loadings of nanowires under the irradiation of laser with the intensity of 98 mW cm^{-2}. (c) Temperature-time curves of the PCL-$W_{18}O_{49}$-0.5 film with different laser intensities.

dynamic mechanical analysis (DMA) stress-controlled programming mode test. Fig. 4a presents a representative curve of PCL-$W_{18}O_{49}$-2 sample (one cycle), with shape fixity (R_f) and shape recovery (R_r) values of 98.3% and 96.1%, respectively. Also, the cycle-to-cycle quantitative assessment verifies the robustness of the composite films (Fig. 4b), with no visible overall strain shift even after four shape memory cycles. This excellent shape memory property enables the film to be employed for repetitive shape memory processes. We attribute the advisable shape memory processes to a well-defined network architecture designed by highly selective thiol-ene reaction [46]. Considering the following photodirected bending experiment, we also conducted the shape memory prop-

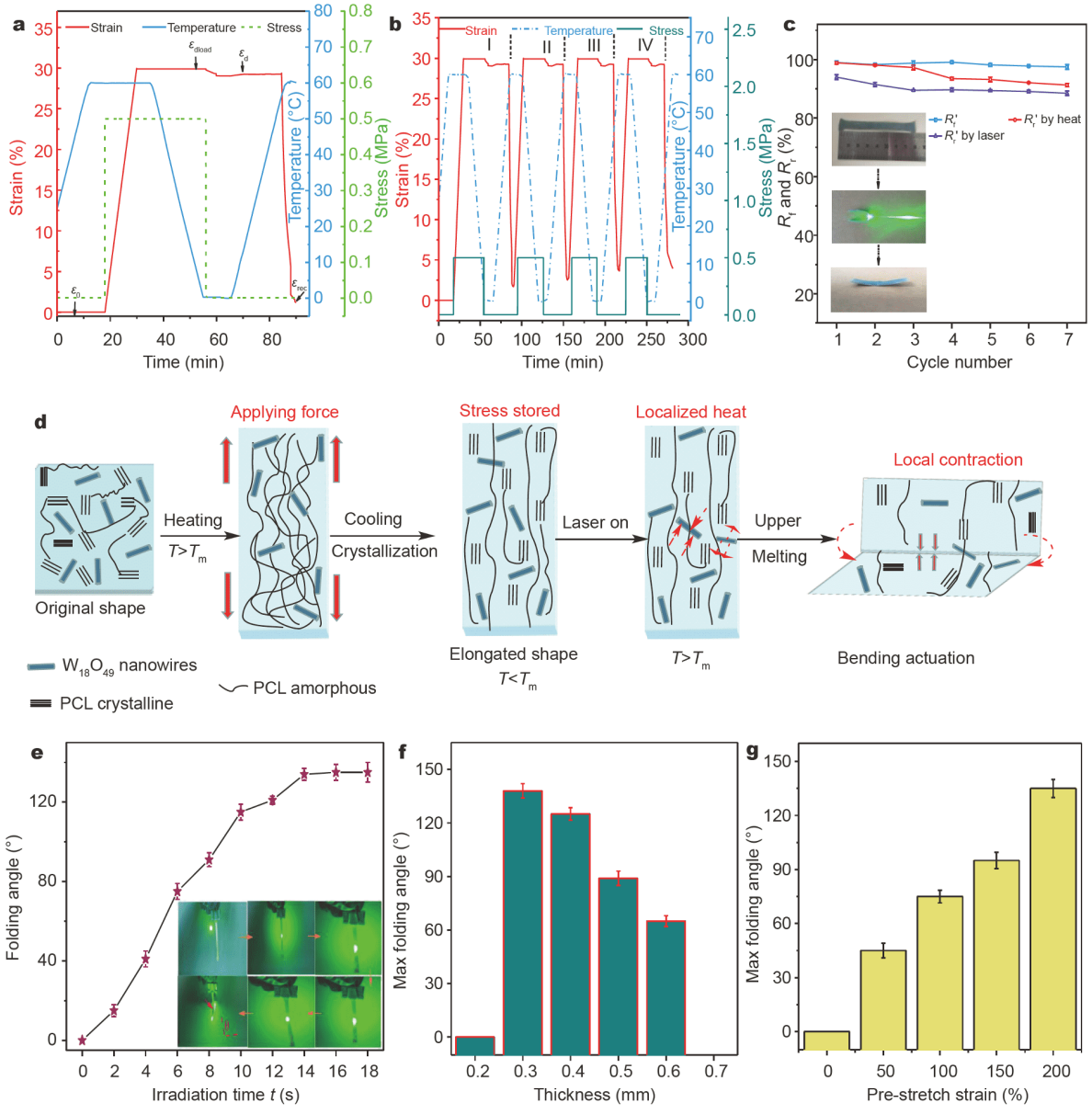

Figure 4 (a) Thermo-induced shape memory effect of the PCL-$W_{18}O_{49}$-2 film with one cycle experiment. (b) Consecutive shape memory effect with four cycles. (c) Four cycles of PCL-$W_{18}O_{49}$-2 film being bent into a temporary U type, and recovered upon heating at 60°C or 98 mW cm^{-2} laser irradiation. (d) Representative mechanism of laser-induced bending deformation of pre-stretched shape memory PCL/$W_{18}O_{49}$ nanowires composite films. (e–g) Parameters involved in folding angle with a laser intensity of 98 mW cm^{-2}. (e) The effect of irradiation time on folding angle; inset shows the real-time pictures of PCL-$W_{18}O_{49}$-2 film with a thickness of 0.3 mm. (f) The effect of thickness on max folding angle with the pre-stretch strain of 200%. (g) The effect of the pre-stretch strain on the folding angle of the PCL-$W_{18}O_{49}$-2 film.

erties based on the folding mode tests. As seen in Fig. 4c, both R_f and R_r are nearly 98% with increasing cycle numbers; however, when the temporary U shape is irradiated with laser rather than heat to trigger its shape recovery, the R_r decreases to 88.5% after seven cycles. We ascribe this decreasing tendency to relatively small size of laser spot that cannot guarantee the entire irradiation when compared with heat. Therefore, the desirable shape memory properties of the composite film are ascribed to the excellent cross-linked network and the excellent photothermal conversion of the PEGylated $W_{18}O_{49}$ nanowires.

As we demonstrate so far, the pre-stretched film can not only achieve the shape memory effect under heat and laser, but also lead to a programable deformation upon irradiation at site-specific regions. We further proposed a possible mechanism to illustrate this. As shown in Fig. 4d, when the sample is heated to above its T_{trans}, the PCL crystalline regions and amorphous domains will melt and the polymer chains become more flexible. In Fig. S5, the materials experience tremendous storage modulus change of up to 2 orders of magnitude upon heating to T_{trans}. Under such circumstance, the initially constrained PCL chains could be stretched in the direction of applied force, and such a deformation can be temporarily fixed once the sample is cooled to room temperature, and thus the strain energy is preserved. Under site-specific illumination with laser, the incorporated $W_{18}O_{49}$ nanowires absorb the light and enable local temperature increasing quickly, thus actuating the elongated composite film with the shape memory effect; however, the absorbed heat in the upper layer of the light-exposed region is different from the bottom layer of the film, causing the shrinkage of only upper layer along the pre-stretched direction and thus providing a driving force (contraction force) towards bending deformation.

We then systematically investigated the basic parameters affecting the bending deformation of the films, including irradiation time, film thickness and pre-stretch strain. As shown in Fig. 4e and Movie S1, the folding angle of the 200% pre-stretched strain film increases to about 135° within 14 s irradiation of 98 mW cm^{-2} laser intensity. After the laser is turned off, the PCL molten part instantaneously recrystallizes and retains the folding angle. It should be noted that the unirradiated bottom layers of the film do not experience the melting-to-recrystallization process and still maintain the pre-stretched shape with pre-stretched stored strain. Regarding the effect of film thickness and pre-stretched strain on the photodirected bending deformation, it also has great impact on the folding angle. In Fig. 4f, the film with a thickness of 0.3 mm can reach a max bending angle and thinner samples appear to generate larger bending angles within the investigated range of thickness, but when the thickness of the pre-stretched film is less than 0.2 mm, the bending deformation behavior cannot occur due to the entire penetration along the thickness direction, thus depriving the temperature gradient within the whole film. Fig. 4g shows that larger strain could also lead to greater folding angle, because the larger pre-stretch strain could store more internal stress to trigger the bending actuation with larger amplitude.

Based on the above results, a certain intended folding angle can be obtained by controlling the site-specific irradiation time, pre-stretch strain as well as the film thickness. The bending deformation occurs in the direction of the incident light due to the contraction of stimulated upper layer. Therefore, the deformation structures of a composite film with different bending directions and bending amplitudes can both be realized by controlling the direction of incident light and the above stated parameters (Fig. S6). A series of 3D complex configurations can be achieved in one pre-stretched film when integrated with kirigami cuts in planar.

As shown in Fig. 5a, we initially obtained a sample with four legs by kirigami cuts in a square sheet, and then stretched each leg along the direction of long axis to 200% strain *via* elasticity, sequentially illuminating the joint area between the middle unstretched square and pre-stretched leg, and then the intermediate part of each leg with 98 mW cm^{-2} laser could deform the shape into a stool-like structure (a-i). Afterwards, by controlling the irradiating position and irradiation time, various other novel configurations (a-ii, iii, iv) with different architectures and heights were obtained step by step. Likewise, Fig. 5b shows the transformation of the 2D triangle to a 3D pyramid-like structure with laser irradiation. Fig. 5c shows the uncovered box will bend to form the folded structure after being triggered by the 98 mW cm^{-2} laser irradiation at site-specific regions. Following the same route, Fig. 5d presents a ladder-like configuration. By stimulating the different site of the elongated region linked with stage of ladder, we obtained the configurations of a ladder in suspended form (d-i, ii) and the ramp form (d-iii, iv). Based on the above results, stepwise-controlled variable shape changes can be realized from 2D planar materials by laser irradiation.

By activating the dynamic covalent bond within the same film, 2D-to-3D shape change could also be achieved based on its reconfigurable characteristic. Reconfigura-

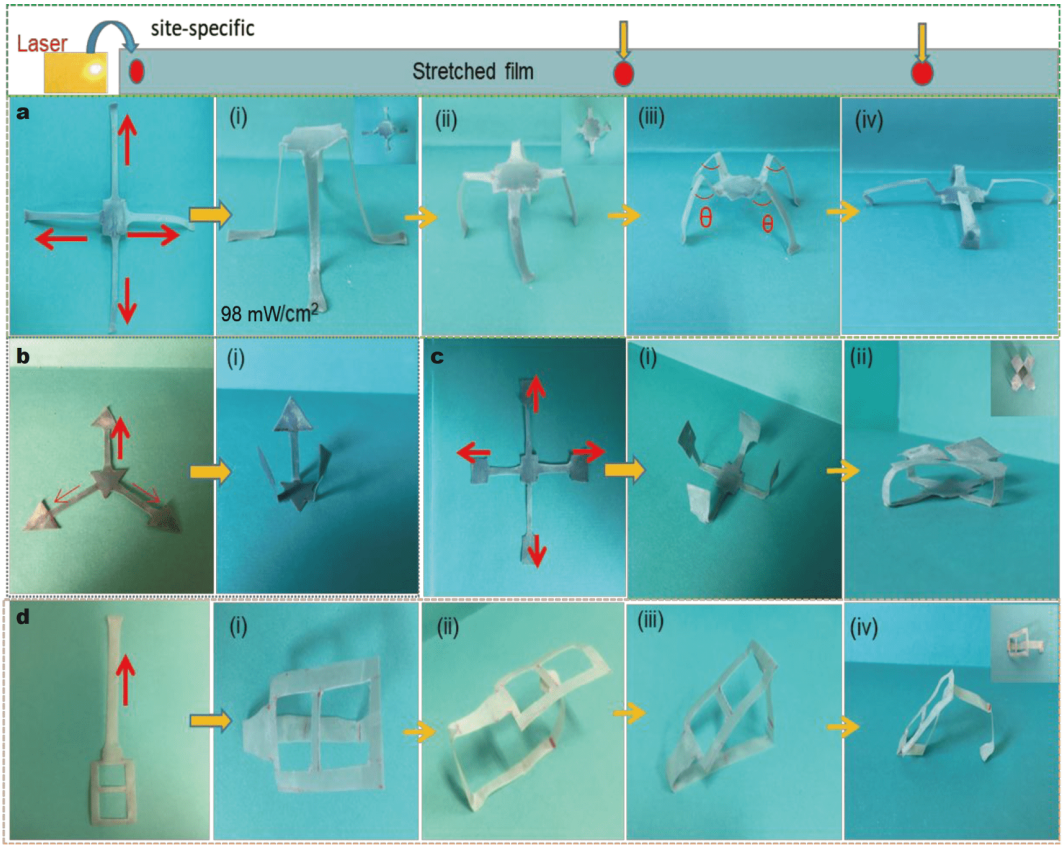

Figure 5 (a) Various stool-like shapes obtained by laser-triggered different sites and side deformations with four legs elongated to 200% strain. (b) A pyramid-like structure obtained by 2D triangle with three legs elongated to 200% strain. (c) The uncovered box with four legs elongated to 200% strain being bent in a folded structure. (d) Various ladder-like configurations. Laser intensity: 98 mW cm^{-2}; film thickness: 0.3 mm. (a-i, ii; c-ii; d-iv) The corresponding top views.

tion test is shown in Fig. 6a with one combined elasticity/plasticity cycle, and no noticeable deterioration in shape memory performance is found after shape reconfiguration, illustrating that the combination of plasticity and elasticity can be achieved in one cross-linked network without any overlap.

Fig. 6b presents the mechanism of elasticity-based and plasticity-based processes. For the conventional elasticity-based shape memory effect, it is elastic deformation caused by the entropy changing that drives the materials to recover to their original shape. While for the plasticity-based changing, upon stretching the film above its T_m, the sample is uniformly deformed at both macroscopic and microscopic scales. With subsequent 130°C heat-treatment, the heat weakens the binding strength of molecular chains. At this stage, if an controlled strain is kept under the external stress and kept for some time, the molecular chains will eventually undergo chain slippage rather than conformational changes, the ester exchange reaction will take place and the network topological structures can be rearranged along with the direction of external stress, which results in the reconfiguration to a new permanent shape (solid state plasticity) [47]. The combined plasticity and elasticity are further visually illustrated in Fig. 6c. A pyramid-like flat sheet with mini-incision is first reconfigured into a new permanent airplane-like origami architecture at 130°C for 45 min, and then the c(ii) is manually fixed to temporary shape c(iii) by virtue of elasticity. When the sample c(iii) is reheated to 60°C or irradiated by a 300 mW cm^{-2} simulated sunlight, it will recover to the reconfigured permanent shape c(ii). Although the two flat shapes c(i) and c(iii) appear geometrically identical, their strain states are different. The flat c(i) is actually in a zero-stress state and the flat c(iii) shape in reality is in a stress-embedded state. It is the internal embedded stress in the 2D plane c(iii) that drives the film to recover to the pre-reconfigured shape upon external stimuli. Following the same route, we next reconfigured a

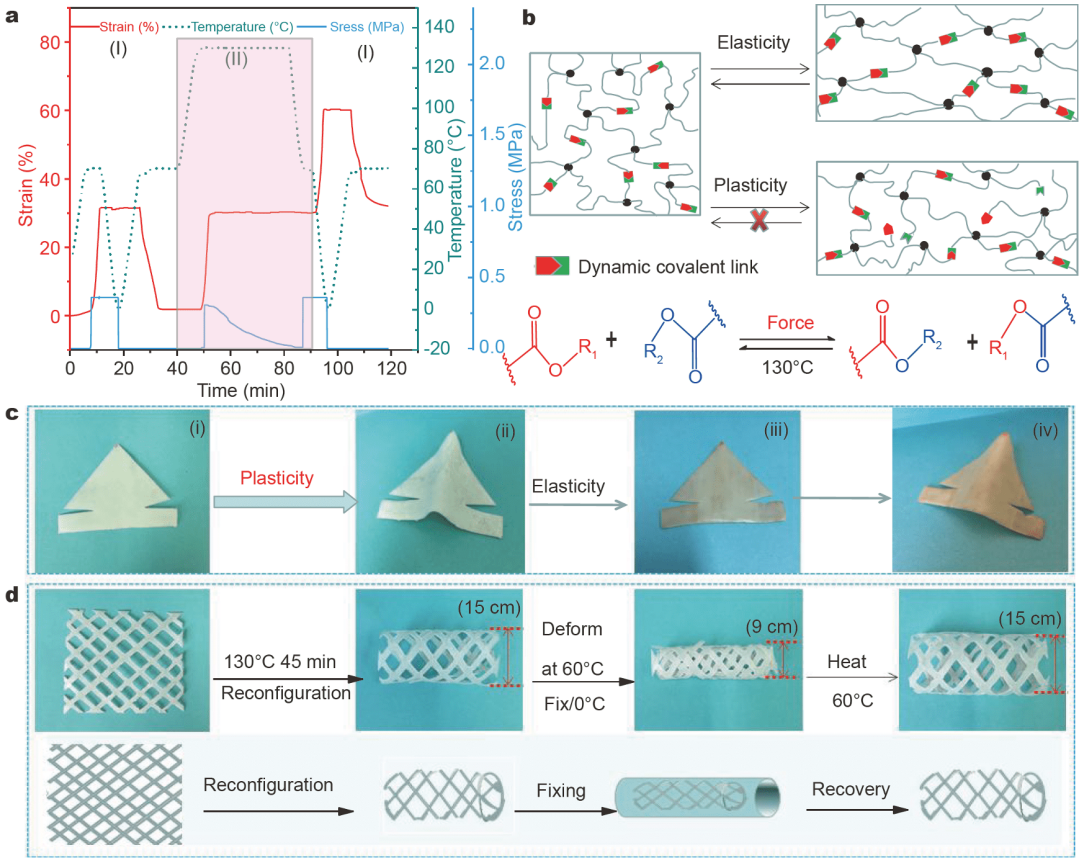

Figure 6 Shape changing characteriaztions of the PCL/$W_{18}O_{49}$ cross-linked networks. (a) The combined elasticity (labeled I) and plasticity (labeled II) cycles. (b) Mechanism of the plasticity and elasticity of the shape memory PCL/$W_{18}O_{49}$ composite film. (c) A visual demonstration of shape reconfiguration, fixing and recovering processes (2D-to-3D, iii-to-iv). (d) Visual presentation of reconfiguring a mesh film into a stent structure and its shape shifting behaviors (upper: real shape changing; below: schematic illustration).

flat mesh into a stent (d-ii) (diameter ~15 mm) by triggering the dynamic transesterification reaction. Afterward, we manually morphed the artificial stent into a volume-contracted stent (diameter ~9 mm) by compressing the reconfigured stent at 60°C and cooling it to 0°C to fix the temporary shape (d-iii). When the volume-contracted stent was warmed to 60°C or irradiated with simulated sunlight, it would get recovered to the reconfigured size (diameter ~15 mm).

CONCLUSIONS

In summary, we reported a facile approach to achieve the transformation of planar 2D structures to complex 3D structures *via* localized laser irradiation. Specifically, by doping PEGylated $W_{18}O_{49}$ nanowires into the composite films, a series of smart PCL/$W_{18}O_{49}$ films with high efficiency of photothermal conversion were obtained. It was found that the concentration of $W_{18}O_{49}$ nanowires in the films and the laser intensity both had influence on the temperature of the film's surface. We demonstrated that the pre-stretched film could undergo an out-of-plane bending deformation behavior upon irradiating site-specific regions with laser. The effects of irradiation time, film thickness as well as pre-stretch strain on the bending amplitudes were systematically investigated, and the results showed that the films with a thickness of 0.3 mm had a max folding angle of 138° and larger pre-stretched strain could lead to greater bending deformation. By integrating these results with kirigami technique, programmed deformations of a pre-stretched 2D film into intricate 3D structure were successfully realized. Finally, based on dynamic transesterification reaction of the system, we demonstrated that such 2D-to-3D transformation can also be realized concurrently by the strategy of solid state plasticity and elasticity. This study paves a solid way for realizing 3D complex deformations of PCL with

remote stimulation and large shape morphing.

Received 2 July 2020; accepted 14 October 2020; published online 4 January 2021

1 Yang P, Zhu G, Xu S, *et al.* A novel shape memory poly(ε-caprolactone) network *via* UV-triggered thiol-ene reaction. J Polym Sci Part B-Polym Phys, 2017, 55: 692–701
2 Tian G, Zhu G, Xu S, *et al.* An investigation on sunlight-induced shape memory behaviors of PCL/TiN composites film. Smart Mater Struct, 2019, 28: 105006
3 Xue J, Wu T, Dai Y, *et al.* Electrospinning and electrospun nanofibers: methods, materials, and applications. Chem Rev, 2019, 119: 5298–5415
4 Nishizawa M. Soft, wet and ionic microelectrode systems. Bull Chem Soc Japan, 2018, 91: 1141–1149
5 Biswas A, Singh AP, Rana D, *et al.* Biodegradable toughened nanohybrid shape memory polymer for smart biomedical applications. Nanoscale, 2018, 10: 9917–9934
6 Herath HMCM, Epaarachchi JA, Islam MM, *et al.* Structural performance and photothermal recovery of carbon fibre reinforced shape memory polymer. Compos Sci Tech, 2018, 167: 206–214
7 Gao H, Li J, Zhang F, *et al.* The research status and challenges of shape memory polymer-based flexible electronics. Mater Horiz, 2019, 6: 931–944
8 Tian G, Zhu G, Ren T, *et al.* The effects of PCL diol molecular weight on properties of shape memory poly(ε-caprolactone) networks. J Appl Polym Sci, 2019, 136: 47055
9 Yang P, Zhu G, Shen X, *et al.* Poly(ε-caprolactone)-based shape memory polymers crosslinked by polyhedral oligomeric silsesquioxane. RSC Adv, 2016, 6: 90212–90219
10 Zheng Y, Li Y, Hu X, *et al.* Biocompatible shape memory blend for self-expandable stents with potential biomedical applications. ACS Appl Mater Interfaces, 2017, 9: 13988–13998
11 Kashif M, Yun B, Lee KS, *et al.* Biodegradable shape-memory poly (ε-caprolactone)/polyhedral oligomeric silsequioxane nanocomposites: Sustained drug release and hydrolytic degradation. Mater Lett, 2016, 166: 125–128
12 Xu S, Chang P, Zhao B, *et al.* Formation of poly(ε-caprolactone) networks *via* supramolecular hydrogen bonding interactions. Chin J Polym Sci, 2019, 37: 197–207
13 Yuan W, Zhou J, Liu K, *et al.* Sequence-rearranged cocrystalline polymer network with shape reconfigurability and tunable switching temperature. ACS Macro Lett, 2020, 9: 588–594
14 Pérez-Camargo RA, Arandia I, Safari M, *et al.* Crystallization of isodimorphic aliphatic random copolyesters: pseudo-eutectic behavior and double-crystalline materials. Eur Polym J, 2018, 101: 233–247
15 Zhang K, Zhao Z, Huang J, *et al.* Self-recoverable semi-crystalline hydrogels with thermomechanics and shape memory performance. Sci China Mater, 2019, 62: 586–596
16 Yao Y, Wang J, Lu H, *et al.* Thermosetting epoxy resin/thermoplastic system with combined shape memory and self-healing properties. Smart Mater Struct, 2016, 25: 015021
17 Kweon H. A novel degradable polycaprolactone networks for tissue engineering. Biomaterials, 2003, 24: 801–808
18 Peng W, Zhang G, Liu J, *et al.* Light-coded digital crystallinity patterns toward bioinspired 4D transformation of shape-memory polymers. Adv Funct Mater, 2020, 30: 2000522
19 Zhang G, Zhao Q, Yang L, *et al.* Exploring dynamic equilibrium of Diels–Alder reaction for solid state plasticity in remoldable shape memory polymer network. ACS Macro Lett, 2016, 5: 805–808
20 Zhao Q, Zou W, Luo Y, *et al.* Shape memory polymer network with thermally distinct elasticity and plasticity. Sci Adv, 2016, 2: e1501297
21 Wang W, Li C, Cho M, *et al.* Soft tendril-inspired grippers: shape morphing of programmable polymer–paper bilayer composites. ACS Appl Mater Interfaces, 2018, 10: 10419–10427
22 Tang J, Yin Q, Qiao Y, *et al.* Shape morphing of hydrogels in alternating magnetic field. ACS Appl Mater Interfaces, 2019, 11: 21194–21200
23 Zhou Y, Tan J, Chong D, *et al.* Rapid near-infrared light responsive shape memory polymer hybrids and novel chiral actuators based on photothermal $W_{18}O_{49}$ nanowires. Adv Funct Mater, 2019, 29: 1901202
24 Li G, Wang S, Liu Z, *et al.* 2D-to-3D shape transformation of room-temperature-programmable shape-memory polymers through selective suppression of strain relaxation. ACS Appl Mater Interfaces, 2018, 10: 40189–40197
25 Yang Y, Pei Z, Li Z, *et al.* Making and remaking dynamic 3D structures by shining light on flat liquid crystalline vitrimer films without a mold. J Am Chem Soc, 2016, 138: 2118–2121
26 Yang Y, Pei Z, Zhang X, *et al.* Carbon nanotube–vitrimer composite for facile and efficient photo-welding of epoxy. Chem Sci, 2014, 5: 3486
27 Yang Y, Ma F, Li Z, *et al.* Enabling the sunlight driven response of thermally induced shape memory polymers by rewritable $CH_3NH_3PbI_3$ perovskite coating. J Mater Chem A, 2017, 5: 7285–7290
28 Chen Q, Yu X, Pei Z, *et al.* Multi-stimuli responsive and multifunctional oligoaniline-modified vitrimers. Chem Sci, 2017, 8: 724–733
29 Chakma P, Konkolewicz D. Dynamic covalent bonds in polymeric materials. Angew Chem Int Ed, 2019, 58: 9682–9695
30 Wu Y, Yang Y, Qian X, *et al.* Liquid-crystalline soft actuators with switchable thermal reprogrammability. Angew Chem Int Ed, 2020, 59: 4778–4784
31 Jiang Z-, Xiao Y-, Tong X, *et al.* Selective decrosslinking in liquid crystal polymer actuators for optical reconfiguration of origami and light-fueled locomotion. Angew Chem Int Ed, 2019, 58: 5332–5337
32 Yang H, Leow WR, Wang T, *et al.* 3D printed photoresponsive devices based on shape memory composites. Adv Mater, 2017, 29: 1701627
33 Ito Y, Tanabe Y, Han J, *et al.* Multifunctional porous graphene for high-efficiency steam generation by heat localization. Adv Mater, 2015, 27: 4302–4307
34 Liu Y, Zhang F, Leng J, *et al.* Remotely and sequentially controlled actuation of electroactivated carbon nanotube/shape memory polymer composites. Adv Mater Technol, 2019, 4: 1900600
35 Yang Q, Peng C, Ren J, *et al.* A near-infrared photoactuator based on shape memory semicrystalline polymers toward light-fueled crane, grasper, and walker. Adv Opt Mater, 2019, 7: 1900784
36 Guler U, Ndukaife JC, Naik GV, *et al.* Local heating with lithographically fabricated plasmonic titanium nitride nanoparticles. Nano Lett, 2013, 13: 6078–6083
37 Wang J, Li Y, Deng L, *et al.* High-performance photothermal conversion of narrow-bandgap Ti_2O_3 nanoparticles. Adv Mater, 2017, 29: 1603730
38 Xi G, Ouyang S, Li P, *et al.* Ultrathin $W_{18}O_{49}$ nanowires with

diameters below 1 nm: synthesis, near-infrared absorption, photoluminescence, and photochemical reduction of carbon dioxide. Angew Chem Int Ed, 2012, 51: 2395–2399
39 Chen Z, Wang Q, Wang H, *et al.* Ultrathin PEGylated $W_{18}O_{49}$ nanowires as a new 980 nm-laser-driven photothermal agent for efficient ablation of cancer cells *in vivo*. Adv Mater, 2013, 25: 2095–2100
40 Tian G, Zhu G, Xu S, *et al.* A novel shape memory poly(ε-caprolactone)/hydroxyapatite nanoparticle networks for potential biomedical applications. J Solid State Chem, 2019, 272: 78–86
41 Li T, Li Y, Wang X, *et al.* Thermally and near-infrared light-induced shape memory polymers capable of healing mechanical damage and fatigued shape memory function. ACS Appl Mater Interfaces, 2019, 11: 9470–9477
42 Miao W, Zou W, Luo Y, *et al.* Structural tuning of polycaprolactone based thermadapt shape memory polymer. Polym Chem, 2020, 11: 1369–1374
43 Rodriguez ED, Luo X, Mather PT. Linear/network poly(ε-caprolactone) blends exhibiting shape memory assisted self-healing (SMASH). ACS Appl Mater Interfaces, 2011, 3: 152–161
44 Zarek M, Layani M, Cooperstein I, *et al.* 3D printing of shape memory polymers for flexible electronic devices. Adv Mater, 2016, 28: 4449–4454
45 Xu Z, Ding C, Wei DW, *et al.* Electro and light-active actuators based on reversible shape-memory polymer composites with segregated conductive networks. ACS Appl Mater Interfaces, 2019, 11: 30332–30340
46 Lewis CL, Meng Y, Anthamatten M. Well-defined shape-memory networks with high elastic energy capacity. Macromolecules, 2015, 48: 4918–4926
47 Yang L, Zhang G, Zheng N, *et al.* A metallosupramolecular shape-memory polymer with gradient thermal plasticity. Angew Chem Int Ed, 2017, 56: 12599–12602

Author contributions Tian G and Zhu G designed the study. Tian G carried out all the experiments. Xu S and Li M helped characterizations of materials and devices, Tian R analyzed the UV-VIS-NIR spectra, Tian G wrote the manuscript and Zhu G revised it. All authors contributed to the general discussion and commented on the final manuscript.

Conflict of interest The authors declare no conflict of interest.

Supplementary information Supporting data are available in the online version of the paper.

Guangming Tian is currently a PhD candidate at the College of Chemistry and Chemical Engineering, Northwestern Polytechnical University. His research interest focuses on shape changing materials, and dynamic covalent bonds in polymer materials.

Guangming Zhu earned his PhD degree from the Northwestern Polytechnical University in 2003, and then he went to Ruhr-University Bochum as a visiting scholar. In 2004, he became a professor at the Northwestern Polytechnical University. His current research interests focus on shape memory polymers, polymer composites, and their applications in aerospace and biomedical engineering.

形状记忆聚己内酯/氧化钨纳米线复合薄膜的光导二维到三维变形结构

田光明[1], 朱光明[1*], 许硕贵[2], 李铭[3], 田仁杰[1]

摘要 形状记忆材料在受到外部刺激时具备可编程的复杂形状和大变形, 该特性对其潜在应用至关重要. 通常情况下将平面二维结构转化为复杂三维结构需要设计非对称的或双层薄膜结构. 在本工作中, 我们提出了一个简单的策略以实现二维到三维结构的转变, 即可以通过激光刺激预拉伸复合薄膜的特定点进而变形成各种预先确定的形状序列. 具体的, 将吸光性$W_{18}O_{49}$纳米线物理掺杂到丙烯酸封端的聚己内酯交联网络中, 当用98 mW cm^{-2}的激光刺激复合薄膜时, 温度梯度和单层薄膜在厚度维度上的单畴取向导致形状记忆聚己内酯/$W_{18}O_{49}$纳米线复合薄膜的面外弯曲变形. 紧接着, 通过调控激光辐照时间、薄膜厚度和预拉伸应变, 可以实现复合薄膜的不同弯曲变形速率和弯曲幅度. 此外, 通过将预拉伸的平面二维状聚合物薄膜与剪纸技术相结合, 复合薄膜在受激后可以朝着更为复杂的三维形状发生变化. 通过激活同一薄膜内的动态酯交换反应也可以实现聚己内酯基复合薄膜的二维到三维形状转化. 因此这种新型薄膜在生物医学器件或软机器人领域具有巨大的应用潜力.

